

1 **Compartmentalization of Axial Seamount's magma reservoir inferred by**
2 **analytical and numerical deformation modeling with realistic geometry**
3

4 **S.R. Slead¹, M. Wei¹, S.L. Nooner², W.W. Chadwick Jr.³, D.W. Caress⁴, and J. Beeson^{3,5}**

5 ¹Graduate School of Oceanography, University of Rhode Island, Narragansett, RI, USA.

6 ²Department of Earth and Ocean Sciences, University of North Carolina Wilmington,
7 Wilmington, NC, USA

8 ³Oregon State University, Cooperative Institute for Marine Ecosystems and Resources Studies,
9 Hatfield Marine Science Center, Newport, OR, USA

10 ⁴Monterey Bay Aquarium Research Institute, Moss Landing, CA, USA

11 ⁵National Oceanic and Atmospheric Administration, Pacific Marine Environmental Laboratory,
12 Newport, OR, USA

13

14 Corresponding author: Sandra Slead (sslead@uri.edu)

15

16 **Key Points:**

- 17 • Uniform pressurization of Axial Seamount's seismically imaged magma reservoir does
18 not adequately fit the observed geodetic data
- 19 • Our models estimate that Axial's magma reservoir inflated by 0.054-0.060 km³ during
20 the inter-eruptive recharge period between 2016-2020
- 21 • Axial's magma reservoir is likely compartmentalized, with magma accumulating in sills
22 along the western-central edge of the magma reservoir

24 **Abstract**

25 Axial Seamount is a submarine volcano on the Juan de Fuca Ridge with enhanced magma supply
26 from the Cobb hotspot. We compare several deformation model configurations to explore how
27 the spatial component of Axial's deformation time series relates to magma reservoir geometry
28 imaged by multi-channel seismic (MCS) surveys. To constrain the models, we use vertical
29 displacements from seafloor pressure sensors and repeat autonomous underwater vehicle (AUV)
30 bathymetric surveys between 2016-2020. We show that implementing the MCS-derived 3D main
31 magma reservoir (MMR) geometry with uniform pressure in a finite element model with uniform
32 elastic host rock properties poorly fits the geodetic data. To test the hypothesis that there is
33 compartmentalization within the MMR that results in heterogeneous pressure distribution, we
34 compare analytical models using various horizontal sill configurations constrained by the MMR
35 geometry. Using distributed pressure sources significantly improves the Root Mean Square Error
36 (RMSE) between the inflation data and the models by an order of magnitude. The RMSE
37 between the AUV data and the models is not improved as much, likely due to larger uncertainty
38 of the AUV data. The models estimate the volume change for the 2016-2020 inter-eruptive
39 inflation period to be between 0.054-0.060 km³ and suggest that the MMR is compartmentalized,
40 with most magma accumulating in sill-like bodies embedded in crystal mush along the western-
41 central edge of the MMR. The results reveal the complexity of Axial's plumbing system and
42 demonstrate the utility of integrating geodetic data and seismic imagery to gain insights into
43 magma storage at active volcanoes.

44

45 **Plain Language Summary**

46 Axial Seamount is a submarine volcano on the Juan de Fuca Ridge (NE Pacific Ocean) with
47 enhanced magma supply from the Cobb hotspot. Its frequent activity and long-term deformation
48 time series covering eruptions in 1998, 2011 and 2015 make it an ideal place to study volcanic
49 processes. Improved magma reservoir modeling at Axial will aid in understanding how magma
50 transport and storage are related to surface deformation, seismicity, and eruption timing. Here we
51 compare several models of Axial's magma reservoir to explore how the spatial component of the
52 observed deformation at Axial compares to seismically imaged magma reservoir geometry. To
53 constrain the models, we use vertical displacements covering an inflation period between 2016-
54 2020, derived from pressure measurements collected at seafloor benchmarks and repeated
55 bathymetric surveys. The models estimate the volume change for the 2016-2020 inflation period
56 to be between 0.054-0.060 km³. Our results suggest that Axial's magma reservoir is
57 compartmentalized, with most magma accumulating in sill-like bodies embedded in crystal
58 mush. The results reveal the spatial complexity of Axial's plumbing system and demonstrate
59 how deformation data and seismic imagery can be used together to gain deeper insights into
60 magma storage at active volcanoes.

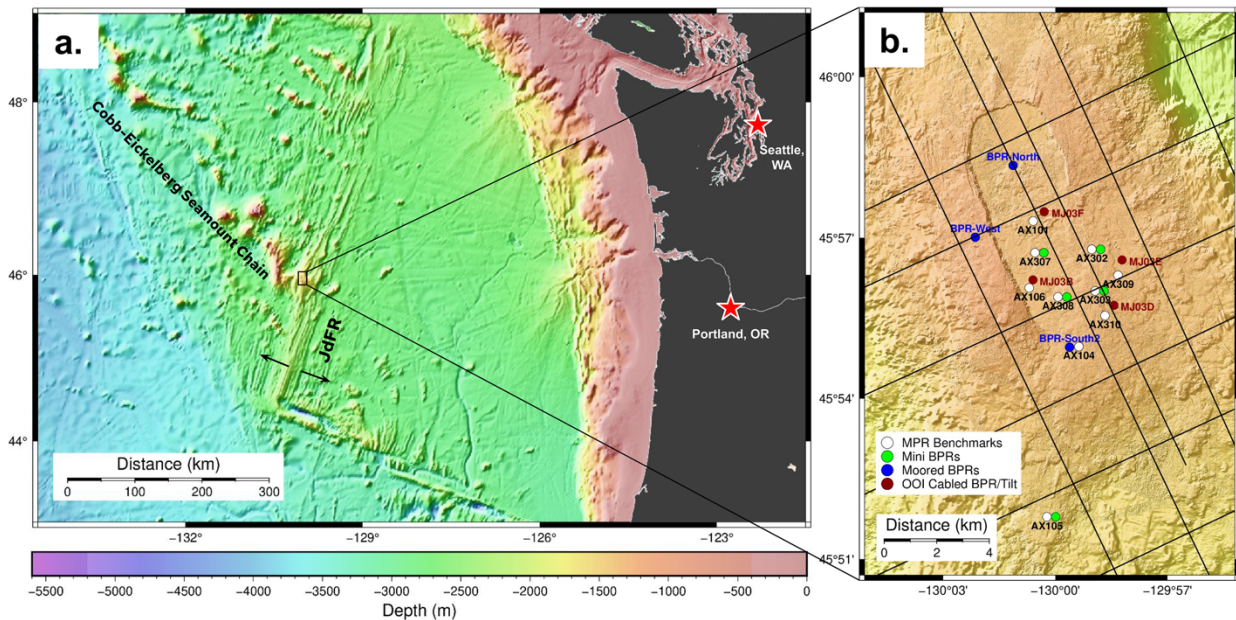
61

62

63

64 **1. Introduction**

65 Axial Seamount is an active submarine volcano located at the intersection of the Juan de
 66 Fuca Ridge and the Cobb hotspot about 500 km west of the Oregon coast in the NE Pacific
 67 (Figure 1). It has erupted at least 52 times over the last 800 years (Clague et al., 2013), most
 68 recently in 1998, 2011, and 2015. A nearly continuous deformation time series from 1998
 69 through the present covering the past 3 eruptions has revealed that Axial exhibits a relatively
 70 repeatable inflation-deflation cycle, which has allowed for two successful eruption forecasts
 71 (Chadwick et al., 2012; Nooner & Chadwick, 2016). Even though Axial itself does not pose a
 72 direct threat to humans because of its remoteness, insight gleaned from observations made at
 73 Axial contribute to a growing body of knowledge about eruptive precursors that can be applied
 74 to more threatening locations (Acocella et al., 2024).



75 **Figure 1.** a) Axial Seamount's tectonic setting at the intersection of the Juan de Fuca Ridge
 76 (JdFR) and the Cobb hotspot. b) Zoom-in of Axial's summit caldera with geodetic
 77 instrumentation as of 2020 labeled. White dots are benchmarks where campaign-style mobile
 78 pressure recorder (MPR) measurements are made, green dots are mini bottom pressure recorders
 79 (BPRs), blue dots are moored BPRs, and red dots are BPRs and tiltmeters connected to the
 80 Ocean Observatories Initiative (OOI) cabled observatory. Black lines are seismic lines (Carbotte
 81 et al., 2008) downward extrapolated by Arnulf et al., 2018 to image the main magma reservoir
 82 (MMR) geometry as used in this study (see Arnulf et al., 2018 for full extent of lines used).
 83

84 Deformation models of Axial have evolved from simple to more complex over the years
 85 as more geodetic data have become available. A point source (Mogi, 1958) was initially used as
 86 the pressure source when few observations were available to constrain models and little was
 87 known about the actual geometry of Axial's magma storage system (Chadwick et al., 2006;
 88 Nooner & Chadwick, 2009). Once more benchmarks for pressure measurements were added and
 89 more analytical model geometries were considered, a steeply dipping prolate spheroid geometry

91 became the best-fit model (Hefner et al., 2020; Nooner & Chadwick, 2016). The prolate spheroid
92 model depth, location, and geometry were somewhat consistent with a set of vertically stacked
93 deep sills later imaged by multi-channel seismic (MCS) data and interpreted by Carbotte et al.,
94 (2020). However, as autonomous underwater vehicle (AUV) repeat bathymetry data (Caress et
95 al., 2020) has begun to provide more spatial coverage and therefore additional constraints for
96 deformation modeling than the limited number of point-pressure observations alone, a
97 rectangular horizontal sill deformation model with about the same outline as the summit caldera
98 has been found to fit both the AUV and pressure data better than a prolate spheroid (Hefner et
99 al., 2021).

100
101 The acquisition of multi-channel seismic (MCS) data at Axial in 2002 (Arnulf et al.,
102 2014, 2018; Carbotte et al., 2020) provided a high-resolution view of the magma reservoir
103 geometry beneath the summit of Axial for the first time. Given the simplicity of the previous
104 analytical deformation models, a logical next step was to investigate how a more realistic
105 geometry of the magmatic system relates to deformation observed at the surface, in order to add
106 more physical meaning to the modeling results. Arnulf et al., (2018) used MCS data to define the
107 3-D geometry and location of the main magma reservoir (MMR) beneath the summit caldera at
108 Axial, as well as a secondary magma reservoir (SMR) located ~ 10 km to the east-southeast. The
109 MMR vertically extends from 1.1-2.8 km depth below seafloor, is slightly offset from Axial's
110 caldera to the east, and extends beyond the caldera to the north and south (Figure 2). The deep
111 stacked sills imaged by Carbotte et al., (2020) are located below the southern half of the MMR
112 between 3-5 km below the seafloor.

113
114 We constructed deformation models constrained by the MMR geometry in several ways.
115 First, we directly used the 3D MMR geometry with uniform internal pressure in a finite element
116 model (FEM), but we found that doing so provides very poor fit to the geodetic data. We then
117 constructed and considered several analytical deformation models as alternatives, including: 1)
118 approximating the MMR shape using one rectangular horizontal sill, 2) approximating the MMR
119 shape using 3 rectangular non-horizontal sills, 3) allowing for non-uniform pressure distribution
120 in a 2D horizontal sill at the average depth of the MMR roof, and 4) allowing for non-uniform
121 pressure distributed over the 3D MMR roof. The models are constrained by the observations of
122 vertical deformation from seafloor pressure data and repeated AUV bathymetric surveys during
123 Axial's current inter-eruption phase between 2016-2020. Our inversion results suggest that the
124 MMR is likely compartmentalized, which is consistent with current thinking on magma reservoir
125 structure.

126
127 **2. Deformation data**

128 Bottom pressure recorders (BPRs) measure pressure at the seafloor; if the seafloor is
129 uplifted, there is less water column above it and therefore lower pressure. Similarly, if the
130 seafloor subsides, the BPR measures higher pressure. The pressure data are converted to depth

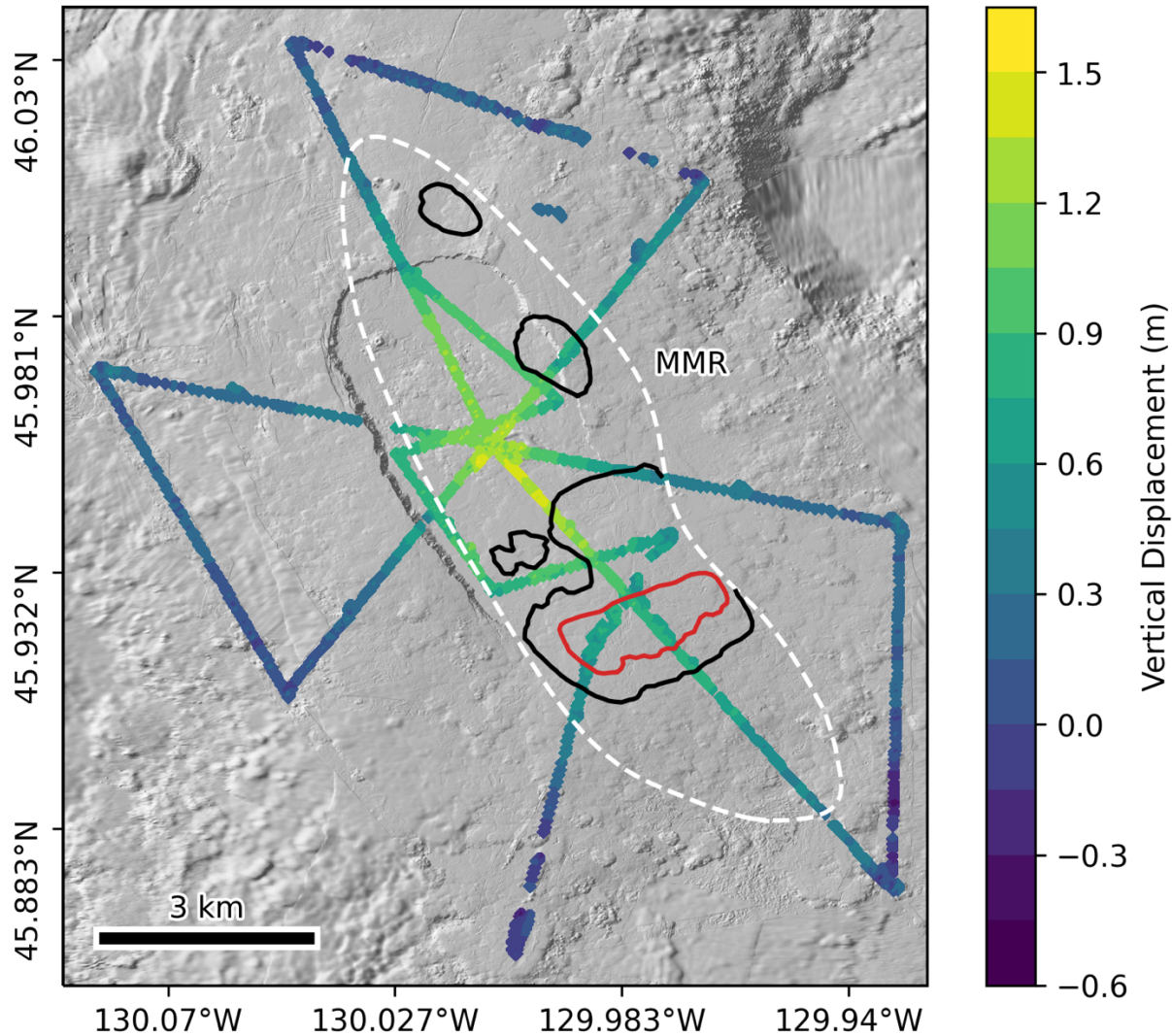
131 after removing tidal signals (Eble et al., 1989). BPRs were deployed at Axial's summit caldera in
132 1998 when Axial's first observed eruption occurred (Chadwick et al., 2013; Dziak & Fox, 1999;
133 Embley et al., 1999; Fox, 1999; Fox et al., 2001). After a two-year gap in coverage, the
134 deformation time series resumed in 2000 with an array of seafloor benchmarks and the time
135 series has been continuous through the present (Figure 1; Chadwick et al., 2006, 2012, 2022;
136 Nooner & Chadwick, 2009, 2016). Since 2000, BPR measurements have been supplemented by
137 measurements from mobile pressure recorders (MPRs), which are used in campaign-style
138 surveys at seafloor benchmarks with a remotely operated vehicle (ROV) every 1-2 years to
139 correct for the BPRs' long-term drift where the two are co-located (Chadwick et al., 2006). We
140 used the MPR data for our study instead of BPR data because there were more MPR
141 measurement locations in 2016-2020 and we are more interested in the spatial component of
142 deformation than the temporal component.

143

144 Bathymetric surveys at 1-m scale have been conducted at Axial since 2006 using
145 multibeam sonar equipped AUVs, first to obtain comprehensive coverage of the volcanic terrain,
146 and then to measure the extent and thickness of lava flows from the 2011 and 2015 eruptions
147 through differencing of repeated surveys (Caress et al., 2012; Chadwick et al., 2016). Beginning
148 after the most recent eruption in 2015, a new sparse pattern of AUV survey lines extending well
149 outside the caldera (Figure 2) was established to measure vertical surface deformation by
150 differencing (Caress et al., 2020); this pattern has been repeated each summer since except 2021.
151 Differencing the repeated components of the surveys reveals vertical surface deformation over a
152 broader area than from the pressure sensors alone. However, compared to the MPR data which
153 has an accuracy of ± 1 cm, the AUV repeat bathymetry data have a lower vertical displacement
154 accuracy of ± 20 cm. We used AUV vertical displacement data between two surveys in 2016 and
155 2020 (Figure 2). An AUV bathymetric survey was also conducted in 2015, but this survey
156 apparently had higher errors than subsequent surveys, because the AUV depth changes between
157 2015-2020 poorly match the MPR depth changes from the same time period. Since MPR
158 measurements were made in 2015 and 2017 (but not in 2016), we estimated the uplift values in
159 2016 at the MPR benchmarks by interpolating between the 2015 and 2017 MPR measurements
160 assuming a linear deformation rate. The BPR record shows that deformation at the center of the
161 caldera during this time period was not entirely linear (Chadwick et al., 2022). The benchmark at
162 the center of the caldera had uplifted by 55 cm from mid-2015 to mid-2016, about 10 cm
163 shallower in summer of 2016 than a linear interpolation would predict (Figure S1 in
164 Supplementary Material). The deformation rate is highest at this benchmark compared to the
165 other benchmarks, so our linear interpolation introduces an additional uncertainty of ≤ 10 cm in
166 the estimated 2016 benchmark depths. Nevertheless, the estimated 2016-2020 depth changes at
167 the benchmarks agree relatively well with the 2016-2020 AUV data (Figure S2 in Supplementary
168 Material).

169

170



171
 172 **Figure 2.** AUV repeat bathymetry data covering 2016-2020. Colors represent depth changes
 173 between AUV surveys. The MMR is outlined with a white dashed line. The shallowest parts of
 174 the MMR roof are shown with depth contours at -1250m and -1500m (below seafloor) in red and
 175 black, respectively. Bathymetry is shown with shaded relief in the background.
 176

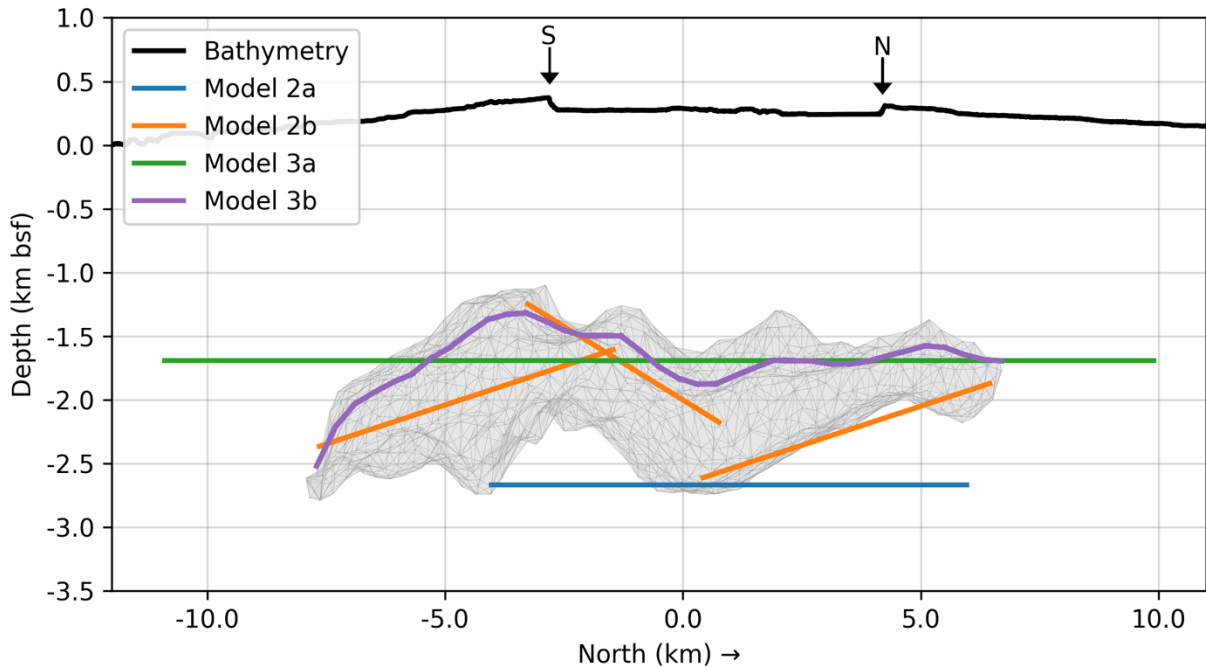
177 We only used deformation data covering the inflation period from 2016 to 2020 to
 178 constrain our models because the main objective of our study is to investigate the spatial
 179 component of the deformation signal and its implications for the underlying magma storage
 180 system. Previous studies have shown that the spatial pattern of inflation does not vary
 181 significantly between different time periods (Nooner & Chadwick, 2016), except for major
 182 episodes of deflation during eruptions when slip on the caldera ring faults may contribute to the
 183 deformation field (Hefner et al., 2020).
 184

185 **3. Deformation modeling**

186 Our objective was to improve upon previous deformation models by reconciling the
 187 MMR geometry with the observed spatial deformation pattern. To do this, we constructed a
 188 series of models with increasing complexity, all constrained/bounded by the MMR. Each is
 189 discussed in detail below. Table 1 contains a summary of model configurations, inversion
 190 methods, and performance. See Figures 3 and 4 for a comparison of model geometries. For all
 191 models, typical mechanical properties were used (Poisson's ratio = 0.25, shear modulus = 30
 192 GPa, Young's modulus = 70 GPa; Turcotte & Schubert, 2014). Although a systematic sensitivity
 193 test of each model to mechanical properties is outside the scope of this study, we found in testing
 194 a range of reasonable mechanical property values for basalt specifically (based on Turcotte &
 195 Schubert 2014) for Model 3b resulted in a volume change estimate range of 0.053629 –
 196 0.053749 km³ (0.22% change). We expect that this would affect the depth and volume change
 197 estimates similarly for those models that allow the source depth(s) to vary.
 198

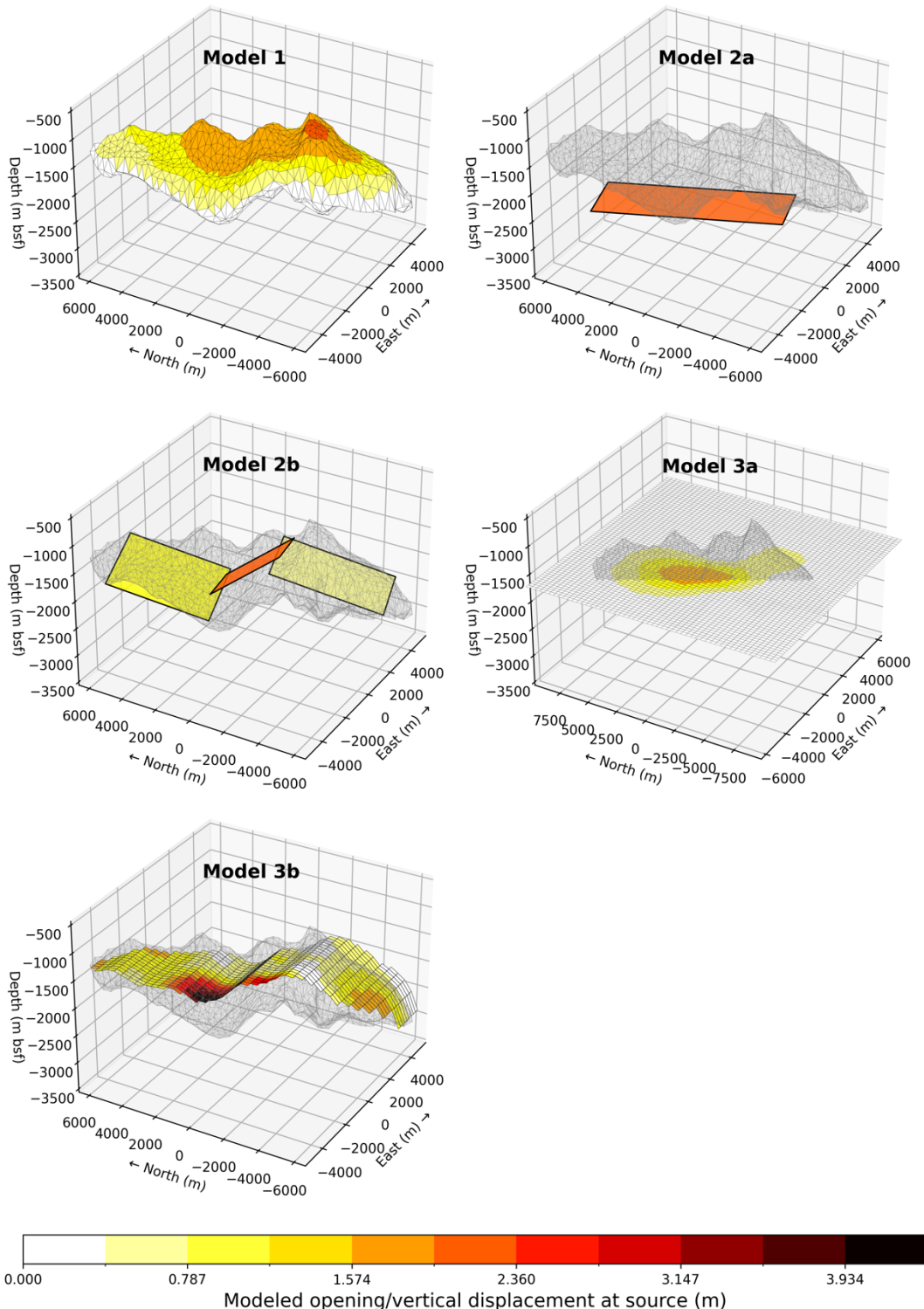
	Model configuration	Inversion method	Volume change (km³)	RMSE_{mp} (m)	RMSE_{auv} (m)
Null model	N/A	N/A	N/A	0.864	0.639
Model 1	FEM, MMR with uniform internal pressure	Parameter search	0.173	0.312	0.254
Model 2a	Analytical, 1 rectangular, horizontal sill	MCMC	0.056	0.059	0.122
Model 2b	Analytical, 3 rectangular, non-horizontal sills	MCMC	0.06	0.047	0.097
Model 3a	Analytical, 2D horizontal grid of Okada sill sources	Least squares regression	0.06	0.009	0.130
Model 3b	Analytical, 3D Okada sill sources draped over MMR roof	Least squares regression	0.054	0.002	0.139

199
 200 **Table 1.** Summary of model configurations, inversion methods, modeled volume changes, and
 201 Root Mean Square Error (RMSE) values between each model and the MPR and AUV data.
 202 RMSE values for a null model with no deformation are shown for comparison.



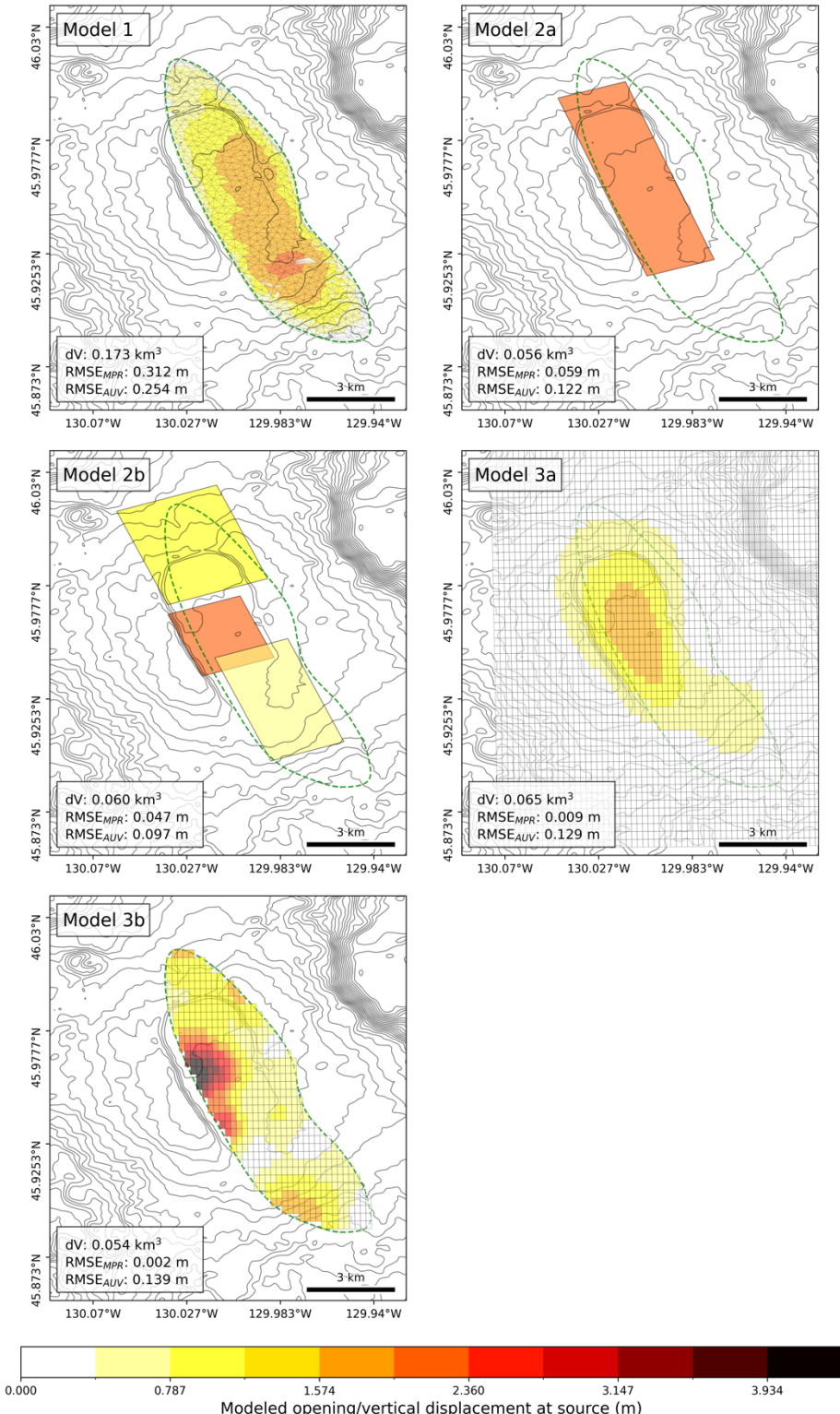
203
204
205
206
207
208
209

Figure 3. North/South cross section showing deformation model geometries investigated in this study. A bathymetric profile taken from North/South across the center of the caldera is also shown (black line); arrows point to the South and North caldera walls. The MMR geometry from Arnulf et al., (2018) is shown as a gray mesh and represents the Model 1 FEM source geometry. The other models are single or multiple combinations of rectangular sills (Okada, 1985; colored lines) with either uniform or distributed (non-uniform) opening. See text for details.



210
211
212
213

Figure 4. Oblique view of model configurations and modeled openings of each pressure source. For Model 1, the color scale represents vertical displacement at the source. For Models 2a-3b, the MMR is shown as a transparent gray mesh to provide context for the model geometries.



214
215
216
217

Figure 5. Map-view of model configurations and modeled openings of each pressure source overlaid on bathymetric contours (contour interval is 35 m). For Model 1, the color scale represents vertical displacement at the source. The MMR is outlined in each plot with a dotted

218 green line. Each model's volume change (dV) and RMSE values between the model and the
219 MPR and AUV data are shown in the lower left corner of each panel.

220

221 **3.1. Model 1a: Finite element model with MMR geometry and uniform pressure**

222 As a first step, we constructed an FEM using the MMR geometry from Arnulf et al., 2018
223 with a uniform pressure source. We started with a 3D point cloud defining the combined MMR
224 roof and floor (see Arnulf et al., 2018 for more detail on how the roof and floor boundaries were
225 defined). A 3D surface was constructed from the point cloud using a ball-pivoting algorithm,
226 which starts with a seed triangle and creates new triangles by pivoting a ball with user-defined
227 radius around the edges until it meets new points (Bernardini et al., 1999). This 3D surface was
228 then loaded into Abaqus/CAE 2020, which we used to carry out the FEM simulations. To
229 validate the FEM methodology, we compared an analytical prolate spheroid model (Yang et al.,
230 1988) to an FEM with a pressurized cavity of the same dimensions and verified that both models
231 predict the same surface deformation (Figure S3 in Supplementary Material).

232

233 The FEM domain measures 50 km long x 50 km wide x 30 km deep and the boundary
234 conditions were specified by a free top surface, a roller constraint on the side surfaces, and a
235 fixed bottom surface. We added bathymetry to the model using GMRT bathymetry data (Ryan et
236 al., 2009). The effect of gravity was accounted for by adding an additional analysis step (prior to
237 pressurization of the source) in which gravitational equilibrium is established by adding a pre-
238 stress defined by hydrostatic equilibrium. This is an 'initial guess' which is used as a starting
239 point to solve for the gravitational force that balances out the pressure force to result in near-zero
240 ground deformation according to a defined threshold. We tested the effect of ocean loading by
241 adding a downward hydrostatic pressure applied to the seafloor and found it to be negligible.

242

243 The MMR was incorporated by subtracting its volume from the domain and applying a
244 uniform internal pressure on the cavity walls. The pressure was varied over many simulations to
245 minimize the combined root-mean-squared error (RMSE) between the modeled surface
246 displacements and the AUV and MPR data.

247

248 **3.2. Models 2a and 2b: Analytical sill models using Bayesian inference**

249 Model 2a is a single rectangular horizontal sill (Okada, 1985) and Model 2b consists of 3
250 non-horizontal rectangular sills constrained by the MMR geometry. We used the Volcanic and
251 Seismic Source Modeling (VSM) package (Trasatti, 2022) to conduct joint inversions using
252 Markov Chain Monte Carlo (MCMC) simulations to estimate the source parameters that produce
253 surface deformation that best fits the AUV and MPR data.

254

255 For Model 2a, all inversion parameters were allowed to vary except for the dip angle of
256 the sill, which was fixed at zero (horizontal). The sill's depth was bounded by the minimum and
257 maximum MMR depth. For Model 2b, the 3-sill geometry was constrained by the MMR
258 geometry by fixing the strike and dip angles in the inversion to follow the general trend of 3

259 main MMR segments (Figures 4 and 5). The locations of the sills were allowed to vary within 3
 260 defined segments of the MMR volume and the sill opening values were allowed to vary freely.
 261 See Table 2 for a summary of fixed and best-fit variable parameters for Models 2a and 2b.
 262

		Centroid Longitude	Centroid Latitude	Centroid depth (m bsf)	Length (m)	Width (m)	Strike	Dip	Opening (m)
Model 2a		-130.0100 ± 258 m	45.9637 ± 110 m	2666 ± 306	2561 ± 1119	9680 ± 253	$341^\circ \pm 2$	0	2.256 ± 0.682
Model 2b	Sill 1	-130.0249 ± 79 m	45.9968 ± 77 m	2241 ± 74	3829 ± 170	5170 ± 115	340°	-7°	1.285 ± 0.041
	Sill 2	-130.0110 ± 83 m	45.9543 ± 97 m	1712 ± 70	2769 ± 166	3475 ± 164	340°	13°	2.071 ± 0.152
	Sill 3	-129.9850 ± 126 m	45.9265 ± 175 m	1985 ± 206	2800 ± 207	5707.36 ± 325	340°	-7°	0.893 ± 0.076

263
 264 **Table 2.** Summary of fixed and best-fit inverted parameters with standard deviations for Models
 265 2a and 2b. The strike angle is the orientation of the plane measured clockwise from North
 266 according to Okada (1985) (i.e., strike = 0 if the plane is oriented North-South and dips to the
 267 East, strike = 90 if the plane is oriented East-West and dips to the South). Fixed parameters have
 268 red shading, parameters allowed to vary within the confines of the MMR geometry have yellow
 269 shading, and parameters allowed to freely vary have green shading.
 270

271 **3.3. Models 3a and 3b: 2D and 3D distributed pressure inversions**

272 Inverting geodetic data to determine variable slip or opening distribution is a standard
 273 method for inferring co-seismic slip on faults (e.g., Moreno et al., 2009) and has also been
 274 applied in volcanic settings (e.g., Grandin et al., 2009). We performed two joint inversions of the
 275 MPR and AUV data following this approach. For Model 3a, we created a 2D horizontal grid of
 276 rectangular sill-patches at the average depth of the MMR roof and extending beyond the MMR
 277 boundary horizontally by 3 km in both the x and y directions. For Model 3b, we gridded the
 278 MMR roof point cloud into rectangular patches where each patch is defined by its position,
 279 length, width, strike, and dip. The patches are allowed to dip in the North/South direction but not
 280 in the East/West direction to create a continuous 3D grid with no gaps; this is appropriate since
 281 there is much more dip variation along the North/South direction of the MMR than there is along
 282 the East/West direction. The depths of the patches were defined by the average MMR roof depth
 283 at that location (Figures 3 and 4).
 284

285 For both Models 3a and 3b, we treated each patch as a rectangular dislocation (Okada,
 286 1985) and inverted for the opening value of each patch. Posed as a forward problem, the
 287 relationship between surface displacements and patch openings can be expressed by the linear
 288 system:

$$289 \quad d = Gm$$

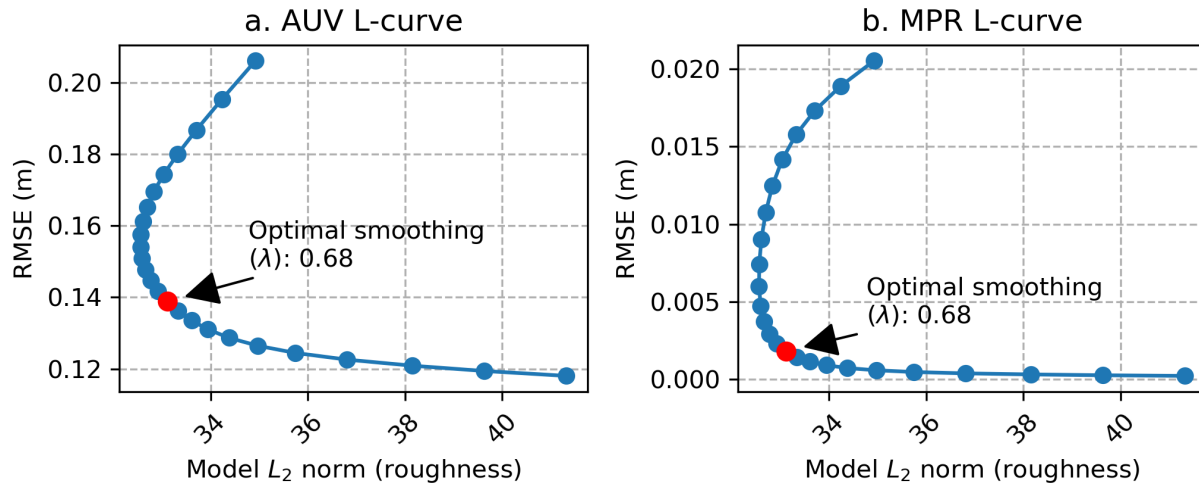
291
292
293
294
295
296
297

where d is the observation vector composed of vertical surface displacements, G is the Green's function matrix, and m is the vector of model parameters (patch openings). G was constructed by computing the expected vertical displacement at every observation point for each patch caused by a unit opening on that patch. To solve for m , we used a regularized linear least squares method which minimizes the objective function, $\phi(m)$:

298
299
300
301
302
303
304
305
306
307

$$\phi(m) = \| W(G \cdot m - d) \|_2^2 + \lambda^2 \| L \cdot m \|_2^2$$

The first term $\| W(G \cdot m - d) \|_2^2$ represents weighted misfit, i.e., the squared Euclidean norm difference between the observed data and the data predicted by the model, where W is a diagonal weight matrix which normalizes the contribution of the MPR and AUV datasets based on the relative uncertainties and the number of relative data points. The second term $\lambda^2 \| L \cdot m \|_2^2$ is the regularization term, where λ is the regularization parameter that controls the smoothness of the model, and L is the regularization matrix. The optimal λ value was chosen using an L-curve, where the preferred smoothness is located at the corner of the curve created by plotting roughness vs. the L2 norm of misfit (Figure 6).



308
309
310
311
312

Figure 6. L-curves showing model roughness vs. Root Mean Square Error (RMSE) as a measure of misfit between the model and the data for (a) the AUV data and (b) the MPR data. The optimal smoothness occurs at the corner of the curve. Example shown is for Model 3b.

313

3.4. Weighing the AUV and MPR data

314
315
316
317
318
319

We weighed the AUV and MPR data on a case-by-case basis for each model due to differences among inversion methods. For Model 1, since the best-fit model was found by a parameter search over uniform pressure values on the MMR surface (all other model parameters were fixed), we calculated the AUV RMSE and MPR RMSE for each iteration then normalized them by dividing each by the maximum RMSE value across all iterations and by the relative uncertainties in the datasets. We then calculated the combined RMSE for each iteration by

320 summing the normalized AUV RMSE and MPR RMSE values. The optimal model was chosen
321 as the model with the lowest combined RMSE value. For Models 2a and 2b, we first weighed the
322 datasets in an MCMC simulation according to their relative uncertainties, then further adjusted
323 the weights over many MCMC simulations to find the weight combination that minimized the
324 combined AUV and MPR RMSE values.

325

326 For Models 3a and 3b, we found a tradeoff between the regularization parameter λ and
327 the relative weights, due to higher noise in the AUV data than in the MPR data. Instead of just
328 normalizing the AUV and MPR datasets using their relative uncertainties, we further normalized
329 them by the number of data points in each dataset. The λ value was then chosen as described
330 above in Section 3.3.

331

332 4. Results

333 We found that Model 1 (uniform pressurization of the 3-dimensional MMR) did not fit
334 either the MPR or AUV data well. This was not unexpected, since the MMR geometry is offset
335 from the caldera to the east while the observed deformation is centered on the caldera. Also, the
336 shallowest features along the MMR roof are located beneath the SE part of the caldera and
337 because of this, the model creates the largest surface deformation there, 4-5 km SE of the caldera
338 center (Figures 2, 4a and 6a). This makes sense intuitively since these shallowest MMR features
339 have less overburden and therefore uplift more readily under uniform pressurization. This result
340 tells us that the observed deformation cannot be simply produced by uniform pressure within the
341 entire MMR, which suggests that perhaps the MMR is compartmentalized with isolated melt
342 pockets that are not well connected.

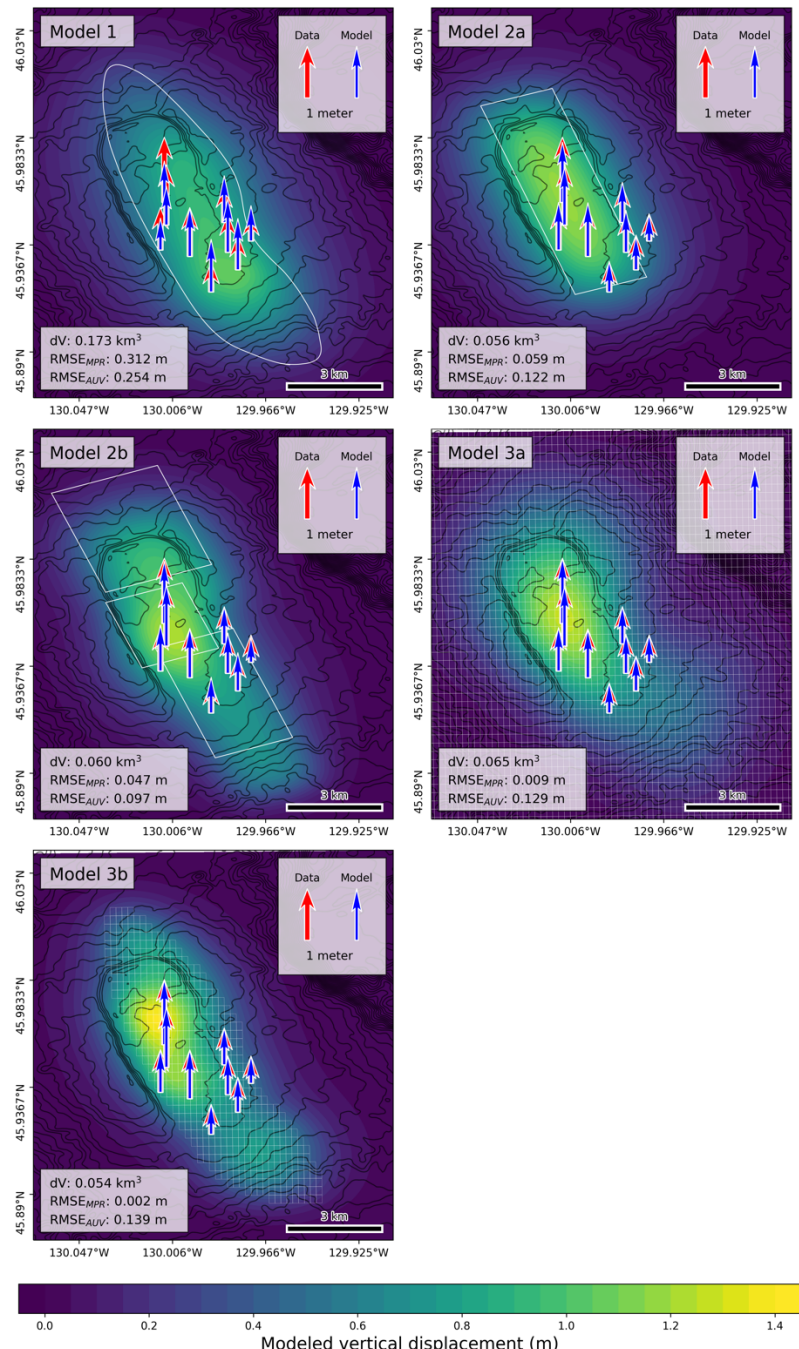
343

344 The other four models, which were developed to test the idea of compartmentalization,
345 showed increasing improvement of fit to the MPR data as more parameters were added. The
346 AUV RMSE values were also improved, but not as much and varied from model to model (Table
347 1). We suspect that this is because of the higher uncertainty associated with the AUV data, which
348 was factored into how the datasets were weighed. To quantify whether the increase in goodness
349 of fit to the data between the models is statistically significant and not due to random fluctuations
350 in the data, we conducted F-tests on each model and its adjacent model with higher complexity
351 using the 95% confidence interval (see Text S2 and Tables S1, S2 in Supplementary Material).
352 We found that the increased goodness of fit to the MPR data across the models is statistically
353 significant. The model pairs for which the AUV RMSE improved with complexity (Model 1 vs.
354 Model 2a, Model 2a vs. Model 2b) also have statistically significant improvement of fit.

355

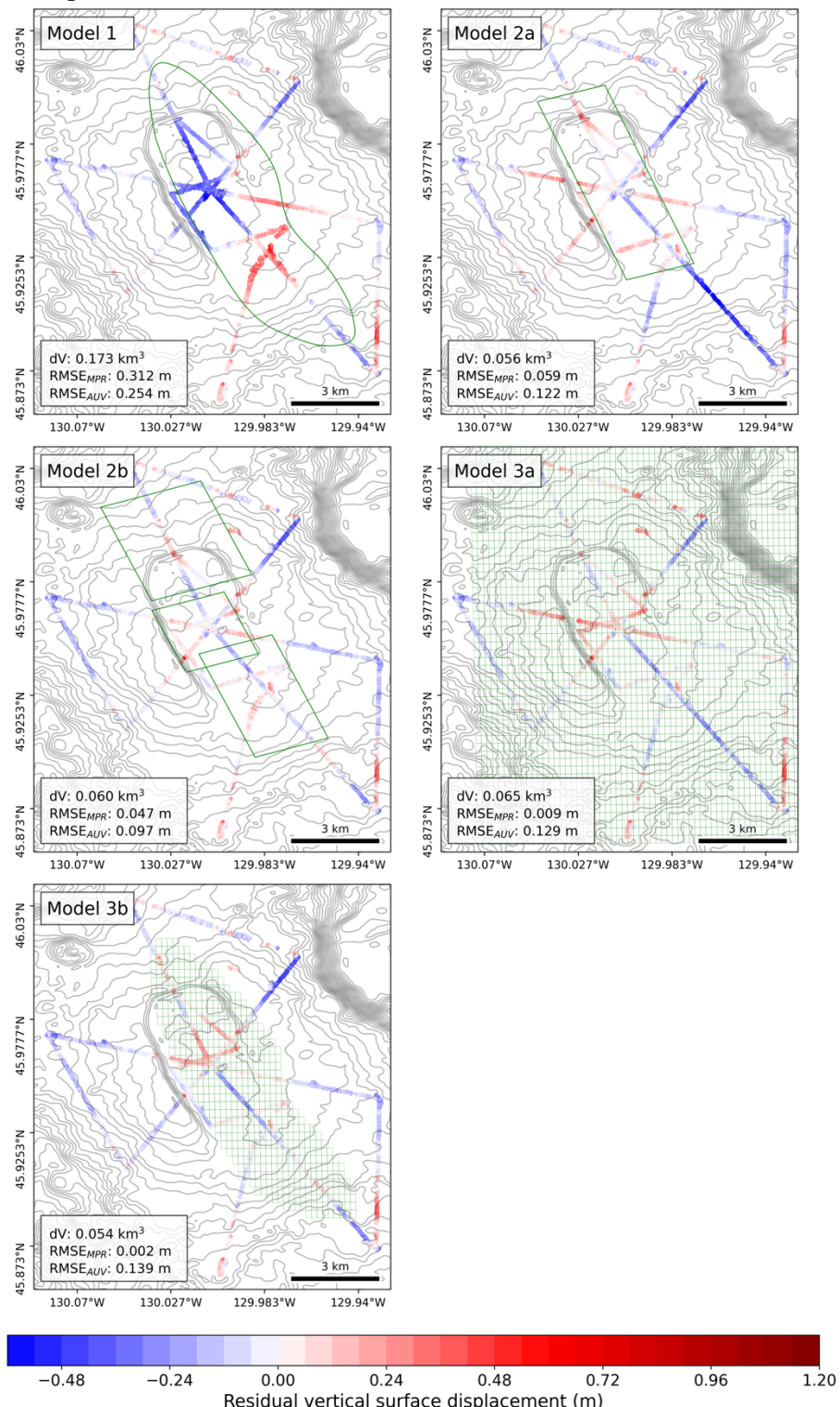
356 Despite differences among model geometries, the models consistently estimated a best-fit
357 volume change of between 0.054-0.060 km³, except for Model 1 which estimated 0.173 km³
358 (Table 1). The best-fit pressure change for Model 1 was 42.4 MPa. Modeled deformation and fit
359 to the MPR data are shown in Figure 7 and AUV repeat bathymetry residuals are shown in

360 Figure 8. In Models 3a and 3b where pressure was allowed to spatially vary, modeled pressure
 361 changes were highest along the western-central edge of the MMR (Figures 4 and 5). There is
 362 also a region of positive pressure change in the southern-most southward dipping region of the
 363 MMR due to a long wavelength deformation signal present in this area in the AUV data.
 364



365
 366 **Figure 7.** Predicted surface vertical deformation for all best-fit models with comparison between
 367 the MPR data (red arrows) and modeled surface displacements (blue arrows). The surface
 368 projection of each model geometry is shown as a white outline. Each model's volume change

369 (dV) and RMSE values between the model and the MPR and AUV data are shown in the lower
 370 left corner of each panel.



371
 372 **Figure 8.** AUV repeat bathymetry residuals plotted by subtracting the modeled displacements
 373 from the AUV data. The surface projection of each model geometry is plotted as a green outline.

374 Each model's volume change (dV) and RMSE values between the model and the MPR and AUV
375 data are shown in the lower left corner of each panel.

376

377 5. Discussion

378 5.1. Model assumptions and limitations

379 All our models assume homogeneous and isotropic elastic half spaces (except for Model
380 1, which includes bathymetry). Masterlark (2007) showed that the presence of layered crustal
381 material can increase source depth estimates when compared to models assuming elastic half
382 spaces with uniform properties. Since Axial's volcanic edifice is composed of lava flows
383 emplaced upon one another over time, there is likely some anisotropy in which stiffness is
384 different in the vertical and lateral directions, which could cause an underestimation of source
385 depths. If those layers are dipping, the symmetry of stress around the pressure source would
386 change (Gudmundsson, 2006), which would in turn affect the symmetry of measured ground
387 displacements. Additional vertical anisotropies such as dikes and/or faults would influence the
388 stress and displacement field similarly. However, since we don't have constraints on these
389 potential vertical anisotropies, it is difficult to quantify the effect for our case.

390

391 We found in sensitivity testing that inclusion of Axial's bathymetry in a finite element
392 model using a prolate spheroid pressure source fixed at a depth of 3.8 km (the best-fit model of
393 Nooner & Chadwick, 2016) can affect the volume change estimate by up to 27% (Figure S3 in
394 Supplementary Material). This effect would increase with shallower source depths (Williams &
395 Wadge, 1998) such as at the depth of the MMR. This result was unexpected because of Axial's
396 relatively modest bathymetric relief, and more work is needed to better understand which
397 bathymetric features (e.g., caldera walls vs surrounding bathymetric features) influence the
398 expression of vertical deformation for a given pressure source geometry.

399

400 Our assumption of elasticity could also affect the modeling results since there may be
401 non-elastic or viscoelastic effects unaccounted for in the models. Numerical modeling
402 implementing viscoelasticity at Mt. Etna has shown that lower pressures can produce the same
403 deformation as elastic models with higher pressure due to viscoelastic relaxation over time (Del
404 Negro et al., 2009). Depending on where this region of viscoelasticity is defined (either above or
405 below the pressure source), this phenomenon could result in either inflation or deflation observed
406 on the surface (Nooner & Chadwick, 2009). Cabaniss et al., 2020 found that non-temperature-
407 dependent elastic rheology requires greater reservoir overpressures to reproduce the observed
408 surface deformation at Axial compared to models that incorporate a temperature-dependent
409 rheology. Additionally, petrological and tomographic studies increasingly show that magma
410 reservoirs are likely composed of discrete melt lenses/sills embedded within a crystal-rich
411 magma mush (Cashman et al., 2017). Magma mush is expected to behave poroelastically or
412 poroviscoelastically (Gudmundsson, 2012; Liao et al., 2018, 2021). Although viscoelastic effects
413 and the presence of magma mush would likely not significantly impact the spatial distribution of
414 modeled pressure changes in our results, it could impact volume change estimates due to magma

415 compressibility. Modeling viscoelastic effects at Axial would be more strongly relevant to the
416 temporal component of the deformation time series, for example to test hypotheses regarding
417 short-term deflation events proposed by Chadwick et al., 2022.

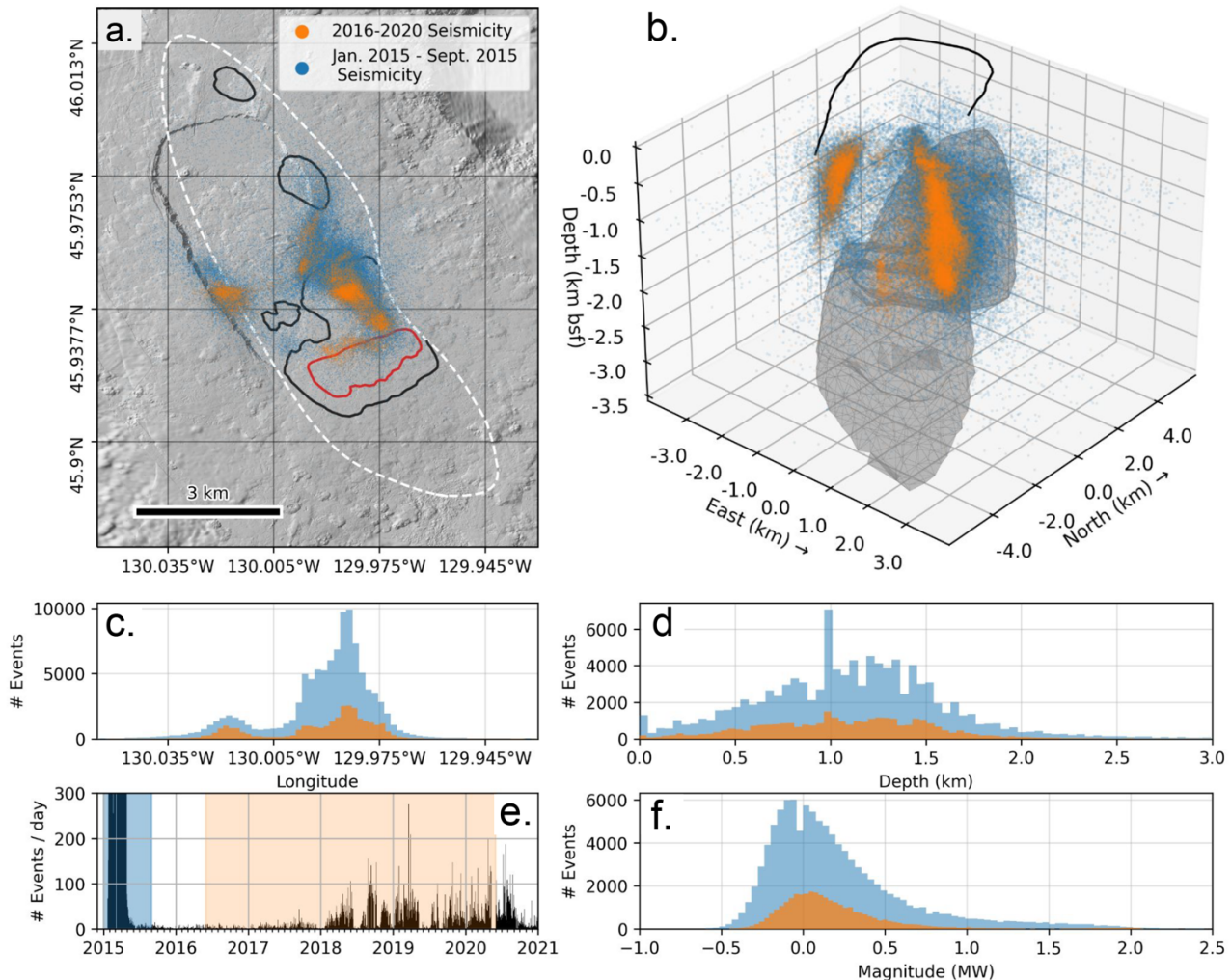
418
419 Because of the MMR's relatively shallow depth, modeled surface deformation is
420 sensitive to roof topography variations at the scale of hundreds of meters to kilometers. The
421 reason Model 1 fits the data poorly is because the shallowest features of the MMR roof are
422 located kilometers away from the largest observed deformation (Figure 2). Our argument that the
423 MMR is not pressurized uniformly therefore relies on the assumptions that 1) the MMR
424 morphology has not changed between the 2002 MCS survey and 2016 and 2) the resolution and
425 quality of the MCS results are adequate for our analysis. It is unlikely that the MMR has changed
426 in morphology since the 2002 MCS survey, since preliminary results from a recent 3D MCS
427 survey in 2019 (Axial 3D expedition MGL1905; Arnulf et al., 2019) suggest that the overall
428 shape and main topographic features have not changed. In addition, the deformation pattern has
429 been consistent throughout the history of geodetic monitoring at Axial, despite the eruption in
430 2015 (Fox 1999; Chadwick et al., 1999, 2006, 2012, 2022; Nooner & Chadwick, 2009, 2016).
431 Uniform pressurization of the MMR might fit the data if the shallowest topographic features
432 were centered beneath the caldera, which would require a change in MMR roof topography of
433 approximately X= 3 km by Y = 6 km by Z = 0.4 km. Therefore, any changes/uncertainties in the
434 MCS results below these dimensions would not alter our conclusions. Changes or uncertainties
435 in the bottom surface topography of the MMR would likely not influence our conclusions, since
436 the displacement at the source for Model 1 (uniform pressurization of the MMR) shows that
437 predicted deformation is not sensitive to these features (Figure 4). This is consistent with
438 findings by Yun et al., 2006, who demonstrated that modeled surface deformation at basaltic
439 calderas is insensitive to the bottom and sides of the model geometry and that it is the upper
440 surface that matters most.

441
442 **5.2. Seismicity**
443 Seismic activity at Axial associated with the 2015 eruption suggests that pre-eruptive
444 inflation and co-eruptive deflation are partly accommodated by slip on outward-dipping caldera
445 ring faults that extend from the near-surface to ~2 km depth (Wilcock et al., 2016; Waldhauser et
446 al., 2020). Levy et al., 2018 divided the 2015 eruption into 3 phases (pre-, syn-, and post-
447 eruption) and used microearthquakes to estimate the cumulative fault slip for each phase. Hefner
448 et al., 2020 used these slip estimates to subtract fault-induced surface deformation from the
449 observed geodetic data prior to performing model inversions and found that the best-fit prolate
450 spheroid source location was shifted laterally by 2.11 km. This demonstrates that ring fault
451 motion at Axial may contribute to the observed surface deformation during eruptions, but likely
452 only 10% or less.

454 To compare the observed seismicity to our deformation model results we plotted
455 earthquakes located during our 2016-2020 inter-eruptive study period and seismicity surrounding
456 the 2015 eruption from the Wilcock et al., 2016 & 2017 earthquake catalog in Figure 9. During
457 2016-2020, seismicity rates started off low (<10 earthquakes per day) for the first 2 years and
458 increased to 10s-100s per day during the next 2 years (Figure 9e), but the amount of expected
459 seismic slip on the ring faults is low, because the magnitude of most earthquakes is also low
460 ($M_w < 2$; Figure 9f).

461
462 It is also possible that magma reservoir inflation is accommodated aseismically by the
463 ring faults. The spatial correlation between the observed surface displacements and the caldera
464 could suggest that the ring faults are active. However, there is little evidence of fault slip in the
465 AUV repeat bathymetry data in the form of sharp offsets along AUV track lines where they cross
466 the faults. There may be some slip masked by the uncertainty in the AUV data (± 20 cm), but it
467 would still only contribute $\sim 10\%$ or less to the observed uplift.

468
469 Regardless of how much of a role the ring faults play in accommodating inflation, it is
470 unlikely that they could accommodate uniform pressurization of the MMR (i.e., Model 1 with
471 ring faults) to produce the observed geodetic data, since most of the surface deformation in
472 Model 1 is to the southeast of the seismicity on the ring faults (Fig. 9a,b). However, if the center
473 of the MMR were pressurized (instead of the west-central edge as in Models 3a and 3b), and the
474 ring faults were allowed to slip, the resulting deformation might fit the geodetic data. An FEM
475 that includes bathymetry, spatially variable pressure, and ring faults that could slip would be
476 most thorough, although the number of free parameters may not be constrainable by the current
477 deformation data. However, recent expansions of the geodetic monitoring network at Axial will
478 be able to better quantify any slip across the caldera faults in the future and will add horizontal
479 displacements.



480
 481 **Figure 9.** Comparison between seismicity during our study period from 2016-2020 in orange
 482 and seismicity associated with the 2015 eruption from January 2015 – September 2015 in
 483 blue. Earthquake data is from Wilcock et al. (2016 & 2017) (a) Map view of the caldera
 484 bathymetry with the MMR outlined in white. Shallowest parts of the MMR roof are shown
 485 with depth contours at -1250m and -1500m (below seafloor) in red and black, respectively.
 486 (b) 3-D perspective view of seismicity compared to the MMR geometry (gray mesh) and
 487 caldera (black line). (c) Histogram of seismic events along longitude. (d) Shows a histogram
 488 of earthquake depths. (e) Time series of seismicity with the 9 months surrounding the 2015
 489 eruption shaded in blue (timespan based on Wilcock et al., 2016) and the 2016-2020 time
 490 period shaded in orange. The maximum number of events per day during the 2015 eruption
 491 (y-axis upper limit) is ~9000. (f) Histogram of earthquake magnitudes (Mw).
 492

493 5.3. Implications for magma storage beneath Axial caldera

494 A best-fitting deformation model cannot reveal the exact geometry of a magma storage
 495 system and should not be interpreted as such; rather, a deformation model can provide the
 496 approximate location and volume changes of the region(s) where the greatest pressure changes

497 occurred during magmatic activity. While our results provide improved horizontal constraints on
498 where magma accumulates between eruptions, there is inherent non-uniqueness among modeled
499 depths due to the tradeoff between depth and pressure. While our best-fit horizontal sill (Model
500 2a) is similar in horizontal geometry to the best-fit horizontal sill found by Hefner et al. (2021),
501 the depth of our sill is deeper at 2.7 km compared to 0.97-1.24 km, which is likely due to
502 differences in inversion methods and/or the tradeoff between depth and pressure.

503

504 Despite this tradeoff, the consistent volume change estimates of 0.054-0.060 km³ among
505 Models 2a-3b suggests that the volume change is not significantly sensitive to model depths
506 within the depth range of the MMR. In addition, we tested an FEM model using the prolate
507 spheroid geometry (the best-fit solution from Nooner & Chadwick, 2016) constrained only by
508 the 2015-2020 MPR data, which resulted in a volume change of 0.077 km³ (Figure S3a in
509 Supplementary Material). Since this included an extra year's worth of inflation compared to the
510 2016-2020 models we show in this study, the estimated volume change for the 2016-2020 time
511 period would be expected to be somewhat lower, more or less consistent with the volume change
512 estimates using geometries constrained by the MMR in Table 1. This demonstrates that the
513 estimated volume change for this inter-eruptive recharge period is not highly sensitive to model
514 geometry, depth, or location.

515

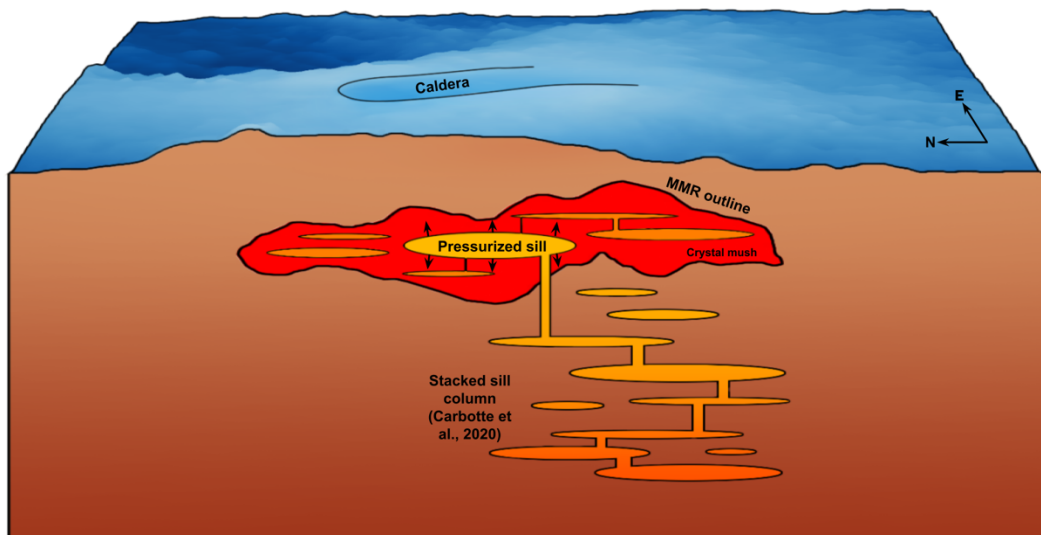
516 The total volume of the shallow magma storage system beneath Axial was estimated by
517 Arnulf et al., 2014 to be 18-30 km³ and the modeled co-eruptive volume change associated with
518 previous eruptions has been estimated to vary between 0.147 – 0.206 km³ using analytical model
519 source depths of 3-3.8 km (Chadwick et al., 1999, 2012; Hefner et al., 2020; Nooner &
520 Chadwick, 2016). Our study models the observed inflation from 2016-2020, during a time when
521 the magma supply rate was initially high, but then waned with time following the 2015 eruption
522 (Chadwick et al., 2022). Given that the magma supply rate is estimated to have varied from >0.1
523 km³/year to <0.01 km³/year during that time period (Chadwick et al., 2022), our volume change
524 estimates are reasonable.

525

526 Mullet & Segall (2022) demonstrated that as the melt fraction of a mushy magma
527 reservoir increases, the deformation caused by a mush-dominated magma storage system is
528 increasingly driven by the overall shape of the mush body, instead of any pressurized melt lens
529 within the mush. If the melt fraction within the MMR is high enough to cause Axial's
530 deformation to be driven by the entire mushy body (instead of individual sills) and if we assume
531 that the MMR is a continuous body, it follows that using the MMR geometry as a pressure
532 source should fit the deformation data. The poor fit to the data of Model 1 as well as the pattern
533 of pressure distribution in Models 2b, 3a and 3b are instead suggestive of compartmentalization
534 of melt within the MMR and a relatively low melt fraction in the surrounding mush (Figure 10).
535 In this context, compartmentalization means that melt bodies within the MMR are not connected
536 hydraulically, at least on time scales that are relevant to the deformation cycle at Axial.

537
538
539
540
541
542
543
544
545

Based on the correlation between the modeled spatial pressure distribution in our models and the MMR outline (the correlation is most apparent in Model 3a), another possibility is an intermediate hypothesis in which one primary sill is pressurized and a large mushy region surrounding the sill that loosely approximates the MMR extent is also pressurized but to a much lesser degree. Both possibilities conflict with melt fraction estimates within the MMR by Arnulf et al., 2018, which suggest that the highest melt fraction is directly beneath the shallowest MMR roof features southeast of the caldera center, with relatively low melt fraction elsewhere.



546
547
548
549

Figure 10. Schematic diagram illustrating possible compartmentalized melt distribution in which sills are emplaced in crystal mush both within and below the MMR at Axial Seamount.

550 The depth of magma residence estimated by petrological analyses (Dreyer et al., 2013) is
551 deeper at 3-6 km than the MMR depth range of 1.1-2.8 km, but is consistent with the deeper
552 system of stacked sills beneath the MMR imaged by Carbotte et al., 2020 extending from 3-5 km
553 depth below seafloor. Since we did not consider deformation sources in this depth range, we
554 cannot rule out contribution to the deformation field of a potential pressure source (or multiple
555 sources) in the deeper stacked sill region. Non-uniqueness among models due to the tradeoff
556 between depth/pressure would likely hinder efforts to resolve pressurization of multiple
557 vertically stacked sills or the combination of compartmentalized MMR pressurization with a
558 source representing the stacked sill region. However, since the stacked sills are exclusively
559 beneath the SSE part of the caldera, they probably cannot produce the observed caldera-centered
560 deformation by themselves.

561
562
563
564

The concept of a “magma domain” was applied to Axial Seamount by Sigmundsson 2016 to describe a crustal volume that hosts magma at a shallow level with varying amounts of melt/mush and pockets with variable connectivity. This concept was also applied to the

565 Bárðarbunga volcanic system in Iceland where caldera collapse in 2014-2015 was modeled using
566 a sill-like magma body within a larger magma domain, which supplied magma to a lateral dike
567 (Sigmundsson et al., 2020). Along with these studies, our results have implications for how
568 deformation models constrained by geodetic data alone should be interpreted, since a best-fit
569 pressure source is likely not representative of the full extent of magma storage beneath a
570 volcano. Although petrological studies suggesting that magma reservoirs are composed of a
571 complex network of melt sills embedded in crystal mush have primarily focused on mafic
572 volcanoes, there is increasing evidence that this may also be the case for some silicic systems
573 (Cashman & Giordano, 2014).

574

575 **6. Conclusions**

576 The ability to accurately forecast volcanic eruptions is an important goal in hazard
577 mitigation research. Linking precursory signals like ground deformation to subsurface processes
578 is therefore essential. With the increase in spatial coverage of Axial's deformation monitoring
579 due to the application of AUV repeat bathymetric surveys, there is now adequate data to justify
580 more complex deformation modeling than what has been done previously. We constructed a
581 suite of numerical and analytical models geometrically constrained by the shape of the
582 seismically imaged MMR to investigate the role of the MMR in creating the observed surface
583 deformation and to test the hypothesis that the MMR is compartmentalized. Although our
584 estimated volume change of 0.054-0.060 km³ for the inflation period between 2016-2020 is
585 reasonable considering previous estimates of inflation, deflation, and eruption volumes, the
586 models make assumptions (flat seafloor, full elasticity, no ring faults) that could influence the
587 volume change and/or depth estimates. Nevertheless, the models with spatially varying pressure
588 (Models 3a and 3b) suggest that magma accumulates during Axial's inter-eruptive recharge
589 periods along the western-central edge of the MMR with some potential additional accumulation
590 in the southern-most southward dipping region of the MMR. Future modeling efforts with
591 additional complexity and more parameters will likely require increased data constraints in the
592 form of higher resolution seismic imagery, AUV repeat bathymetry with lower uncertainty,
593 and/or the additional constraint of horizontal deformation measurements.

594

595 **Acknowledgements**

596 Collection of data used in this study was funded by the National Science Foundation (NSF;
597 awards OCE-1736926, 1736882, and 1737019) and the David and Lucille Packard Foundation.
598 M. Wei was supported by NSF award 2025563. The authors are grateful to Adrien Arnulf for
599 providing the MMR top and bottom horizon geometry, to Suzanne Carbotte for helpful
600 discussions, and to Milena Marjanović and Freysteinn Sigmundsson for their careful reviews
601 which helped to improve the manuscript. The authors also thank the crews of R/V Thompson,
602 R/V Kilo Moana, R/V Zephyr, and R/V Rachel Carson for their support at sea, the ROV Jason
603 team (WHOI National Deep Submergence Facility) for conducting the MPR surveys, and the

604 operational teams of AUV Sentry (WHOI National Deep Submergence Facility) and the MBARI
605 Mapping AUVs for conducting the AUV surveys.

606

607 **Open Research**

608 The code and data used for this research can be found at <https://zenodo.org/records/10785669>
609 (Slead, 2024). Academic licensing for Abaqus software is provided by Simulia, Dassault
610 Systèmes. The VSM software used for analytical modeling can be found at
611 <https://github.com/EliTras/VSM> (Trasatti, 2022).

612

613

614

615 **References**

- 616 Acocella, V., Ripepe, M., Rivalta, E., Peltier, A., Galetto, F., & Joseph, E. (2024). Towards
617 scientific forecasting of magmatic eruptions. In *Nature Reviews Earth and Environment*
618 (Vol. 5, Issue 1, pp. 5–22). Springer Nature. <https://doi.org/10.1038/s43017-023-00492-z>
- 619 Arnulf, A. F., Harding, A. J., Kent, G. M., Carbotte, S. M., Canales, J. P., & Nedimović, M. R.
620 (2014). Anatomy of an active submarine volcano. *Geology*, 42(8), 655–658.
621 <https://doi.org/10.1130/G35629.1>
- 622 Arnulf, A. F., Harding, A. J., Kent, G. M., & Wilcock, W. S. D. (2018). Structure, Seismicity,
623 and Accretionary Processes at the Hot Spot-Influenced Axial Seamount on the Juan de Fuca
624 Ridge. *Journal of Geophysical Research: Solid Earth*, 123(6), 4618–4646.
625 <https://doi.org/10.1029/2017JB015131>
- 626 Arnulf, A. F. , Harding, A. J. , Sastrup S., Kell, A. M. , Kent, G. M. , Carbotte, S. M. , Canales,
627 J. P. , Nedimovic, M. R. , Bellucci M., Brandt, S. , Cap, A. , Eischen, T. E. , Goulain, M. ,
628 Griffiths, M. , Lee, M. , Lucas, V. , Mitchell, S. J. , & Oller, B. (2019). Imaging the internal
629 workings of Axial Seamount on the Juan de Fuca Ridge. In *American Geophysical Union,*
630 *Fall Meeting 2019, abstract #OS51B-1483.*
- 631 Bernardini, F., Mittleman, J., Rushmeier, H., Silva, C., & Taubin, G. (1999). The ball-pivoting
632 algorithm for surface reconstruction. *IEEE Transactions on Visualization and Computer*
633 *Graphics*, 5(4), 349–359. <https://doi.org/10.1109/2945.817351>
- 634 Cabaniss, H. E., Gregg, P. M., Nooner, S. L., & Chadwick, W. W. (2020). Triggering of
635 eruptions at Axial Seamount, Juan de Fuca Ridge. *Scientific Reports*, 10(1), 1–11.
636 <https://doi.org/10.1038/s41598-020-67043-0>
- 637 Carbotte, S. M., Arnulf, A., Spiegelman, M., Lee, M., Harding, A., Kent, G., Canales, J. P., &
638 Nedimović, M. (2020). Stacked sills forming a deep melt-mush feeder conduit beneath axial
639 seamount. *Geology*, 48(7), 693–697. <https://doi.org/10.1130/G47223.1>
- 640 Carbotte, S. M., Nedimović, M. R., Canales, J. P., Kent, G. M., Harding, A. J., & Marjanović, M.
641 (2008). Variable crustal structure along the Juan de Fuca Ridge: Influence of on-axis hot
642 spots and absolute plate motions. *Geochemistry, Geophysics, Geosystems*, 9(8).
643 <https://doi.org/10.1029/2007GC001922>

- 644 Caress, D. W., Clague, D. A., Paduan, J. B., Chadwick, W. W., Nooner, S. L., & Thomas, H. J.
645 (2020). Vertical Deformation of the Axial Seamount Summit from Repeated 1-m Scale
646 Bathymetry Surveys Using AUVs. In *American Geophysical Union, Fall Meeting 2020*,
647 *abstract #V040-0017*.
- 648 Caress, D. W., Clague, D. A., Paduan, J. B., Martin, J. F., Dreyer, B. M., Chadwick, W. W.,
649 Denny, A., & Kelley, D. S. (2012). Repeat bathymetric surveys at 1-metre resolution of lava
650 flows erupted at Axial Seamount in April 2011. *Nature Geoscience*, 5(7), 483–488.
651 <https://doi.org/10.1038/ngeo1496>
- 652 Cashman, K. v., & Giordano, G. (2014). Calderas and magma reservoirs. In *Journal of*
653 *Volcanology and Geothermal Research* (Vol. 288, pp. 28–45). Elsevier.
654 <https://doi.org/10.1016/j.jvolgeores.2014.09.007>
- 655 Cashman, K. V., Sparks, R. S. J., & Blundy, J. D. (2017). Vertically extensive and unstable
656 magmatic systems: A unified view of igneous processes. *Science*, 355(6331).
657 <https://doi.org/10.1126/science.aag3055>
- 658 Chadwick, W. W., Clague, D. A., Embley, R. W., Perfit, M. R., Butterfield, D. A., Caress, D.
659 W., Paduan, J. B., Martin, J. F., Sasnett, P., Merle, S. G., & Bobbitt, A. M. (2013). The
660 1998 eruption of Axial Seamount: New insights on submarine lava flow emplacement from
661 high-resolution mapping. *Geochemistry, Geophysics, Geosystems*, 14(10), 3939–3968.
662 <https://doi.org/10.1002/ggge.20202>
- 663 Chadwick, W. W., Embley, R. W., Milburn, H. B., Meinig, C., & Stapp, M. (1999). Evidence for
664 deformation associated with the 1998 eruption of Axial Volcano, Juan de Fuca Ridge, from
665 acoustic extensometer measurements. *Geophysical Research Letters*, 26(23), 3441–3444.
666 <https://doi.org/10.1029/1999GL900498>
- 667 Chadwick, W. W., Nooner, S. L., Butterfield, D. A., & Lilley, M. D. (2012). Seafloor
668 deformation and forecasts of the April 2011 eruption at Axial Seamount. *Nature*
669 *Geoscience*, 5(7), 474–477. <https://doi.org/10.1038/ngeo1464>
- 670 Chadwick, W. W., Nooner, S. L., Zumberge, M. A., Embley, R. W., & Fox, C. G. (2006).
671 Vertical deformation monitoring at Axial Seamount since its 1998 eruption using deep-sea
672 pressure sensors. *Journal of Volcanology and Geothermal Research*, 150(1–3), 313–327.
673 <https://doi.org/10.1016/j.jvolgeores.2005.07.006>
- 674 Chadwick, W. W., Paduan, J. B., Clague, D. A., Dreyer, B. M., Merle, S. G., Bobbitt, A. M.,
675 Caress, D. W., Philip, B. T., Kelley, D. S., & Nooner, S. L. (2016). Voluminous eruption
676 from a zoned magma body after an increase in supply rate at Axial Seamount. *Geophysical*
677 *Research Letters*, 43(23), 12,063–12,070. <https://doi.org/10.1002/2016GL071327>
- 678 Chadwick, W. W., Wilcock, W. S. D., Nooner, S. L., Beeson, J. W., Sawyer, A. M., & Lau, T.
679 K. (2022). Geodetic Monitoring at Axial Seamount Since Its 2015 Eruption Reveals a
680 Waning Magma Supply and Tightly Linked Rates of Deformation and Seismicity.
681 *Geochemistry, Geophysics, Geosystems*, 23(1). <https://doi.org/10.1029/2021GC010153>
- 682 Clague, D. A., Dreyer, B. M., Paduan, J. B., Martin, J. F., Chadwick, W. W., Caress, D. W.,
683 Portner, R. A., Guilderson, T. P., McGann, M. L., Thomas, H., Butterfield, D. A., &

- 684 Embley, R. W. (2013). Geologic history of the summit of Axial Seamount, Juan de Fuca
685 Ridge. *Geochemistry, Geophysics, Geosystems*, 14(10), 4403–4443.
686 <https://doi.org/10.1002/ggge.20240>
- 687 Del Negro, C., Currenti, G., & Scandura, D. (2009). Temperature-dependent viscoelastic
688 modeling of ground deformation: Application to Etna volcano during the 1993-1997
689 inflation period. *Physics of the Earth and Planetary Interiors*, 172, 299–309.
690 <https://doi.org/10.1016/j.pepi.2008.10.019>
- 691 Dreyer, B. M., Clague, D. A., & Gill, J. B. (2013). Petrological variability of recent magmatism
692 at Axial Seamount summit, Juan de Fuca Ridge. *Geochemistry, Geophysics, Geosystems*,
693 14(10), 4306–4333. <https://doi.org/10.1002/ggge.20239>
- 694 Dziak, R. P., & Fox, C. G. (1999). The January 1998 Earthquake swarm at Axial Volcano, Juan
695 de Fuca Ridge: Hydroacoustic evidence of seafloor volcanic activity. *Geophysical Research
696 Letters*, 26(23), 3429–3432. <https://doi.org/10.1029/1999GL002332>
- 697 Eble, M. C., Gonzalez, F. I., Mattens, D. M., Milburn, H. B., Mosbacher, R. A., Knauss, J. A., &
698 Fletcher, J. O. (1989). *Instrumentation, field operations, and data processing for PMEL
699 deep ocean bottom pressure measurements*.
- 700 Embley, R. W., Chadwick, W. W., Clague, D., & Stakes, D. (1999). 1998 eruption of axial
701 volcano: Multibeam anomalies and sea-floor observations. *Geophysical Research Letters*,
702 26(23), 3425–3428. <https://doi.org/10.1029/1999GL002328>
- 703 Fox, C. G. (1999). In situ ground deformation measurements from the summit of Axial Volcano
704 during the 1998 volcanic episode. *Geophysical Research Letters*, 26(23), 3437–3440.
705 <https://doi.org/10.1029/1999GL900491>
- 706 Fox, C. G., Chadwick, W. W., & Embley, R. W. (2001). Direct observation of a submarine
707 volcanic eruption from a sea-floor instrument caught in a lava flow. *Nature* 2001 412:6848,
708 412(6848), 727–729. <https://doi.org/10.1038/35089066>
- 709 Grandin, R., Socquet, A., Binet, R., Klinger, Y., Jacques, E., De Chabalier, J. B., King, G. C. P.,
710 Lasserre, C., Tait, S., Tapponnier, P., Delorme, A., & Pinzuti, P. (2009). September 2005
711 Manda hararo-dabbahu rifting event, Afar (Ethiopia): Constraints provided by geodetic
712 data. *Journal of Geophysical Research: Solid Earth*, 114(8).
713 <https://doi.org/10.1029/2008JB005843>
- 714 Gudmundsson, A. (2006). How local stresses control magma-chamber ruptures, dyke injections,
715 and eruptions in composite volcanoes. *Earth-Science Reviews*, 79(1–2), 1–31.
716 <https://doi.org/10.1016/j.earscirev.2006.06.006>
- 717 Gudmundsson, A. (2012). Magma chambers: Formation, local stresses, excess pressures, and
718 compartments. *Journal of Volcanology and Geothermal Research*, 237–238, 19–41.
719 <https://doi.org/10.1016/j.jvolgeores.2012.05.015>
- 720 Hefner, W. L., Noonan, S. L., Chadwick, W. W., & Bohnenstiehl, D. R. (2020). Revised
721 Magmatic Source Models for the 2015 Eruption at Axial Seamount Including Estimates of
722 Fault-Induced Deformation. *Journal of Geophysical Research: Solid Earth*, 125(4),
723 e2020JB019356. <https://doi.org/10.1029/2020JB019356>

- 724 Hefner, W., Nooner, S. L., Chadwick, W. W., Caress, D. W., Paduan, J. B., Bohnenstiehl, D. R.,
725 & Clague, D. A. (2021). Deformation Models for the 2015-Eruption and Post-Eruption
726 Inflation at Axial Seamount from Repeat AUV Bathymetry. In *AGU Fall Meeting 2021*,
727 held in New Orleans, LA, 13-17 December 2021, id. V45B-0138.
- 728 Levy, S., Bohnenstiehl, D. R., Sprinkle, P., Boettcher, M. S., Wilcock, W. S. D., Tolstoy, M., &
729 Waldhauser, F. (2018). Mechanics of fault reactivation before, during, and after the 2015
730 eruption of Axial Seamount. *Geology*, 46(5), 447–450. <https://doi.org/10.1130/G39978.1>
- 731 Liao, Y., Soule, S. A., & Jones, M. (2018). On the Mechanical Effects of Poroelastic Crystal
732 Mush in Classical Magma Chamber Models. *Journal of Geophysical Research: Solid Earth*,
733 123(11), 9376–9406. <https://doi.org/10.1029/2018JB015985>
- 734 Liao, Y., Soule, S. A., Jones, M., & Le Mével, H. (2021). The Roles of Heat and Gas in a Mushy
735 Magma Chamber. *Journal of Geophysical Research: Solid Earth*, 126(4).
736 <https://doi.org/10.1029/2020JB019395>
- 737 Masterlark, T. (2007). Magma intrusion and deformation predictions: Sensitivities to the Mogi
738 assumptions. *Journal of Geophysical Research*, 112(B6), B06419.
739 <https://doi.org/10.1029/2006JB004860>
- 740 Mogi, K. (1958). Relations between the eruptions of various volcanoes and the deformations of
741 the ground surfaces around them. *Bull. Earthq. Res. Inst.*, 36, 99–134.
742 <https://ci.nii.ac.jp/naid/10017329458/>
- 743 Moreno, M. S., Bolte, J., Klotz, J., & Melnick, D. (2009). Impact of megathrust geometry on
744 inversion of coseismic slip from geodetic data: Application to the 1960 Chile earthquake.
745 *Geophysical Research Letters*, 36(16). <https://doi.org/10.1029/2009GL039276>
- 746 Mullet, B., & Segall, P. (2022). The Surface Deformation Signature of a Transcrustal, Crystal
747 Mush-Dominant Magma System. *Journal of Geophysical Research: Solid Earth*, 127(5).
748 <https://doi.org/10.1029/2022JB024178>
- 749 Nooner, S. L., & Chadwick, W. W. (2009). Volcanic inflation measured in the caldera of axial
750 seamount: Implications for magma supply and future eruptions. *Geochemistry, Geophysics,
751 Geosystems*, 10(2). <https://doi.org/10.1029/2008GC002315>
- 752 Nooner, S. L., & Chadwick, W. W. (2016). Inflation-predictable behavior and co-eruption
753 deformation at Axial Seamount. *Science*, 354(6318), 1399–1403.
754 <https://doi.org/10.1126/SCIENCE.AAH4666>
- 755 Okada, Y. (1985). Surface deformation due to shear and tensile faults in a half-space. *Bulletin of
756 the Seismological Society of America*, 75(4), 1135–1154.
- 757 Ryan, W. B. F., Carbotte, S. M., Coplan, J. O., O’Hara, S., Melkonian, A., Arko, R., Weissel, R.
758 A., Ferrini, V., Goodwillie, A., Nitsche, F., Bonczkowski, J., & Zemsky, R. (2009). Global
759 multi-resolution topography synthesis. *Geochemistry, Geophysics, Geosystems*, 10(3).
760 <https://doi.org/10.1029/2008GC002332>
- 761 Sigmundsson, F. (2016). New insights into magma plumbing along rift systems from detailed
762 observations of eruptive behavior at Axial volcano. In *Geophysical Research Letters* (Vol.

- 763 43, Issue 24, p. 12,423-12,427). Blackwell Publishing Ltd.
764 <https://doi.org/10.1002/2016GL071884>
- 765 Sigmundsson, F., Pinel, V., Grapenthin, R., Hooper, A., Halldórsson, S. A., Einarsson, P.,
766 Ófeigsson, B. G., Heimisson, E. R., Jónsdóttir, K., Gudmundsson, M. T., Vogfjörd, K.,
767 Parks, M., Li, S., Drouin, V., Geirsson, H., Dumont, S., Fridriksdottir, H. M.,
768 Gudmundsson, G. B., Wright, T. J., & Yamasaki, T. (2020). Unexpected large eruptions
769 from buoyant magma bodies within viscoelastic crust. *Nature Communications*, 11(1).
770 <https://doi.org/10.1038/s41467-020-16054-6>
- 771 Slead, S. (2024). Data and Code for Modeling Axial Seamount [Dataset] [Software]. Zenodo.
772 <https://doi.org/10.5281/zenodo.10785669>
- 773 Trasatti, E. (2022). Volcanic and Seismic Source Modeling: An Open Tool for Geodetic Data
774 Modeling [Software]. *Frontiers in Earth Science*, 10.
775 <https://doi.org/10.3389/feart.2022.917222>
- 776 Turcotte, D. L., & Schubert, G. (2014). *Geodynamics* (3rd ed.). Cambridge University Press.
- 777 Waldhauser, F., Wilcock, W. S. D., Tolstoy, M., Baillard, C., Tan, Y. J., & Schaff, D. P. (2020).
778 Precision Seismic Monitoring and Analysis at Axial Seamount Using a Real-Time Double-
779 Difference System. *Journal of Geophysical Research: Solid Earth*, 125(5), 1395–1399.
780 <https://doi.org/10.1029/2019JB018796>
- 781 Wilcock, W. S. D., Tolsoy, M., Waldhauser, F., Garcia, C., Tan, Y. J., Bohnenstiehl, D. R.,
782 Caplan-Auerbach, J., Dziak, R. P., Arnulf, A. F., & Mann, M. E. (2016). Seismic
783 constraints on caldera dynamics from the 2015 Axial Seamount eruption. *Science*,
784 354(6318), 1395–1399.
- 785 Wilcock, W. S. D., Waldhauser, F., & Tolstoy, M. (2017). Catalogs of earthquake recorded on
786 Axial Seamount from January, 2015 through November, 2015 (investigators William
787 Wilcock, Maya Tolstoy, Felix Waldhauser). In *Interdisciplinary Earth Data Alliance*.
- 788 Williams, C., & Wadge, G. (1998). The effects of topography on magma chamber deformation
789 models: Application to Mt. Etna and radar interferometry. *Advances in Difference
790 Equations*, 25(10), 1549–1552. <https://doi.org/10.1186/s13662-019-2194-1>
- 791 Yang, X. M., Davis, P. M., & Dieterich, J. H. (1988). Deformation from inflation of a dipping
792 finite prolate spheroid in an elastic half-space as a model for volcanic stressing. *Journal of
793 Geophysical Research*, 93(B5), 4249–4257. <https://doi.org/10.1029/JB093iB05p04249>
- 794 Yun, S., Segall, P., & Zebker, H. (2006). Constraints on magma chamber geometry at Sierra
795 Negra Volcano, Galápagos Islands, based on InSAR observations. *Journal of
796 Volcanology and Geothermal Research*, 150(1–3), 232–243.
797 <https://doi.org/10.1016/j.jvolgeores.2005.07.009>
- 798
- 799 **References from the supporting information**
- 800
- 801 Menke, W. (2012). Describing Inverse Problems. In *Geophysical Data Analysis: Discrete
802 Inverse Theory* (p. 111-112). Elsevier. [https://doi.org/10.1016/b978-0-12-397160-9.00001-1](https://doi.org/10.1016/b978-0-12-397160-
803 9.00001-1)